International Journal of Early Childhood Special Education (INT-JECSE)
DOI:10.48047/intjecse/v13i2.21237 ISSN: 1308-5581 Vol 13, Issue 02 2021

SOC COMPATIBLE 1T1C FERAM MEMORY ARRAY BASED ON FERROELECTRIC HF0. 5ZR0. 5O2

[1]P.RAMA THULASI,[2]M.CHENNAIAH
Department Of ECE
St. Johns College of Engineering & Technology, Errakota, Yemmiganur

Abstract—Prior research have shown that the film thickness scaling of ferroelectric Hf0.5Zr0.5O2 (HZO) enables hafnium-based onetransistor and one-capacitor (1T1C) ferroelectric random-access memory (FeRAM) to achieve improved cycle tolerance for severe breakdown, while operating at lower voltages. This study expands upon earlier research by conducting a comprehensive analysis of current studies on FeRAM-related devices, specifically focusing on the scaling of film thickness. We conducted an experimental study to confirm the advantage of film thickness scaling in a 1T1C FeRAM array with different HZO thicknesses of 8 nm and 10 nm. We used small capacitors with areas of 0.20, 0.40, and 1.00 μm2 under practical operating conditions. Our results show that the 8-nm sample with a smaller capacitance area exhibited higher reliability, providing the first evidence of the cycling tolerance advantage. In order to validate the outcome, time zero dielectric breakdown (TZDB) and time dependent dielectric breakdown (TDDB) experiments were performed on samples measuring 8-nm and 10a-nm, respectively.
The index terms used in this study are capacitor, ferroelectric random-access memory, hafnium oxide, thickness scaling, and zirconium oxide.

I. INTRODUCTION

In recent years, there has been an increase in demand for lowpower and high-density embedded memory devices that support cache memory applications. In 2011, ferroelectricity of Sidoped HfO2 (HfSiO2) was discovered, revealing that a polarorthorhombic phase in the crystalized HfSiO2 film enables ferroelectricity [1], [2]. HfO2-based ferroelectric devices have been reported extensively owing to their low energy consumption during active and stand-by operation and compatibility with the CMOS logic fabrication process [3].

Various types of ferroelectric devices have been suggested including ferroelectric field-effect transistors (FeFETs), onetransistor and one-capacitor ferroelectric random-access memories (1T1C FeRAMs), and ferroelectric tunnel junctions (FTJs). To switch the polarity of a ferroelectric film, it is necessary to apply a voltage greater than the coercive field; reducing the ferroelectric film thickness will contribute to lowering the applied voltage. Table I presents a comparison of the basic parameters of the FeFET, FTJ, and 1T1C FeRAM with their ferroelectric materials, including thickness.

In the case of FeFETs, a high-density memory array with nondestructive readout operation and support for multibit-level memory has been reported [4]. However, the insulating layer that is easily generated on the Si surface causes charge trapping, leading to dielectric breakdown, which in turn degrades cycling tolerance. The ferroelectric film thickness is optimized considering the ferroelectricity of the ferroelectric layer and dielectric breakdown of the insulator caused by divided voltage [5]–[7]. FTJs allow nondestructive readout operation with a two-terminal structure as resistive random access memories (ReRAMs) that consist of metal/ferroelectric/metal (MFM). An intermediate interfacial layer is usually fabricated as a tunneling layer on the metal electrodes [8]–[10]. Compared with other ReRAMs, these devices have the potential to be high-density and low-power neuromorphic devices owing to their high resistance during the multiply-accumulate operation. The thickness of the ferroelectric film is optimized to control the modulation of the barrier height through the ferroelectric materials and the intermediate interfacial layer while taking the tunneling current into account.

In terms of 1T1C FeRAMs, many researchers have reported that MFM capacitor exhibits high cycling tolerance for hard breakdown owing to the good interfacial property between the ferroelectric layer and metal electrodes [11]–[13]. In addition, anti-ferroelectric type (AFE-type) 1T1C FeRAMs comprising tetragonal phase dominant HfO2-based ferroelectric material have been proposed. The remanent polarization of the AFEtype 1T1C FeRAMs becomes smaller than that of ferroelectric type 1T1C FeRAMs, but low operation voltage with high endurance would be obtained [14], [15]. On the other hand, film thickness scaling allows ferroelectric type (FE-type) 1T1C FeRAMs to reduce the

operating voltage more flexibly compared with FeFETs or FTJs, owing to the thickness optimization between the ferroelectric layer and insulation layer. The strategy of low-voltage operation using film thickness scaling was comprehensively reported, revealing a 1.2 V operation with 4-nm-thick Hf0.5Zr0.5O2 (HZO) using a large single capacitor [16].

We have reported a 64 kbit FE-type 1T1C FeRAM with higher cycling tolerance for hard breakdown with lower voltage operation via HZO film thickness scaling [17], [18]. In this study, we present an extension of the previous work on investigating film thickness scaling and experimentally demonstrating its effect by array-level endurance analysis for the first time. Furthermore, time zero dielectric breakdown (TZDB) and time-dependent dielectric breakdown (TDDB) on single large capacitors with 10-nm-thick HZO (10-nm) and 8- nm-thick HZO (8-nm) samples were conducted to support the result.

Table I. Feature comparison.

Device	FeFET	FTJ	1T1C FeRAM (FE-type)		
	[4]	[8]	[12]	[16]	[17]
Nondestructive read	✔	✔			
Low write voltage (≤ 2.0V)				✔	✔
Endurance (> 10^6)			✔	✔	✔
Retention (85°C 10years)	✔		✔	✔	✔
Array operation	✔		✔		✔
Material	Si:HfO_2	Si:HfO_2	Zr:HfO_2	Zr:HfO_2	Zr:HfO_2
Thickness	7- 9 nm	5 - 7 nm	10 nm	4 nm	8 nm

II. EXPERIMENT

A. Device Fabrication

A 64 kbit FE-type 1T1C FeRAM array was integrated by using 130-nm CMOS technology [12]. The structure of a capacitor under bitline (CUB) was adopted to the memory array. Planer type of MFM capacitors comprising PVD-TiN/ALDHf0.5Zr0.5O2/CVD-TiN were stacked on the contact plug of the planer transistor. Two different HZO samples with thickness values of 8 nm and 10 nm were prepared to investigate arraylevel film thickness scaling. The HZO thickness was confirmed by ellipsometer measurement. Rapid thermal annealing (RTA) at 600 °C was performed on both the HZO samples to obtain a significant ferroelectric property with high remanent polarization (2Pr) from a memory window point of view. If insufficient thermal budget is applied to the capacitors, the film would contain more anti-ferroelectric or amorphas domains, resulting in lower remanent polarization. The RTA did not degrade the characteristics of the CMOS transistors post backend-of-line (BEOL) process [13]. Fig. 1 shows a device structure of the test chip for optical micrograph in Fig. 1 (a) and cross-sectional scanning electron microscopy image of a memory cell which has a capacitor of size 1.00 µm2 in Fig. 1 (b). Four different mats, which had 64 kbits MFM capacitors, were mounted on the same chip with each capacitor in the memory cell having a size of 0.06, 0.20, 0.40, and 1.00 µm2 , respectively. The intrinsic ferroelectricity and TDDB investigations of the MFM capacitors were electrically investigated using a single large MFM capacitor with an area of 1,000 µm2 and was composed of 1,000 capacitors (each of area 1 µm2) connected in parallel for both the 10-nm and 8-nm samples.

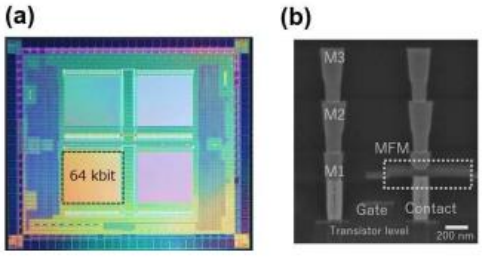

Fig. 1. (a) Optical micrograph of the FE-typed 1T1C FeRAM with 4 mats consisting of different sizes of MFM capacitors, (b) Crosssectional SEM image of a 1T1C memory cell with a capacitance area of 1.00 µm2 [12].

B. Validation of 1T1C FeRAM Array

Fig. 2 (a) shows a schematic figure of the 1T1C FeRAM array with a sense amplifier (SA), which is simplified to explain an operation principle. The capacitance of MFM (CFE) was controlled by

applying the voltage of a word line (WL), bitline (BL), and plate line (PL). Fig. 2 (b) illustrates the definition of CFE as C0 (when reading data0) or C1 (when reading data1). Thus, higher voltage change (ΔVBL) is obtained when reading data1 according to CFE. The reference voltage (VREF) can be modified by externally applying a voltage or internally generating a voltage using the reference capacitance (CREF).

Fig. 3 demonstrates the timing diagrams of a step pulse sensing scheme for data0 and data1 on the 1T1C memory cells: (a) simulation results and (b) experimental waveforms. A high value of ΔVBL or VREF was successfully activated as simulation results when reading data0 or data1.

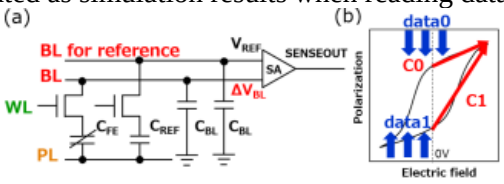

Fig. 2. (a) Schematic illustration simplified to a 1T1C memory cell connected to SA with a reference capacitor. (b) Definition of the CFE as C0 (when reading data0) or C1 (when reading data1) [13].

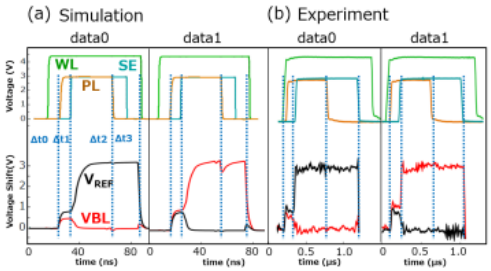

Fig. 3. Validation result of a read operation for a 1T1C FeRAM memory cell for reading data0 and reading data1. (a) Timing diagrams of the simulation results (b) Experimental waveforms [13].

III. RESULTS AND DISCUSSION

A. Ferroelectricity of the film

Fig. 4 demonstrates the presence of ferroelectric orthorhombic phases in both the 10-nm and 8-nm samples via grazing-incidence X-ray diffraction (GIXRD). The intensities related to the ferroelectric orthorhombic phases were similar in both cases at around 30°, while a slightly higher intensity of the monoclinic related phase was observed for the 10-nm samples at around 28°. Fig. 5 shows the remanent polarization of the MFM for both samples that are characterized by polarization versus voltage measurements with a maximum applied electric field of 3 MV/cm. The ferroelectric hysteresis indicates the presence of a ferroelectric orthorhombic phase in each case. A slightly higher remanent polarization (2Pr, ~32 μC/cm2) was observed on the 8-nm sample than on the 10-nm (2Pr, ~27 μC/cm2) sample, which is in agreement with the GIXRD results.

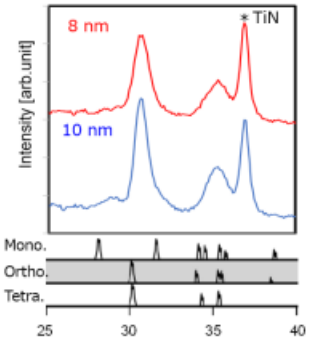

Fig. 4. GIXRD spectra of the MFM capacitors on 8-nm and 10-nm HZO samples.

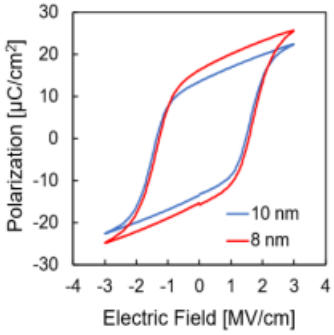

Fig. 5. P-E characteristics of the 8-nm (red) and 10-nm (blue) samples using single large MFM capacitors at 1 kHz after 100 cycles over an area of 1,000 μm2 .

B. Reliability characterization using a single capacitor

Reliability analyses were conducted on the intrinsic ferroelectric films of 8-nm and 10-nm samples using MFM capacitors with a total area of 1,000 μm2 each. The electric breakdown electric field (EBD) was 4.8 MV/cm for the 8-nm sample, while 4.2 MV/cm on the 10-nm sample based on J–E measurements (Fig. 6). This phenomenon can be explained by a similar theory with regard to the metal/oxide/silicon (MOS) structure, which shows better breakdown tolerance on thinner SiO2 from lower electron energy for a given field [16], [20].

The TDDB characteristics of the MFM capacitor were obtained by current–time trace test (Fig. 7). Constant voltage stress values of 3.3 V (3.3 MV/cm), 3.4 V (3.4 MV/cm), 3.5 V (3.5 MV/cm), and 3.6 V (3.6 MV/cm) were applied to the 10- nm samples, while stress values of 3.1 V (3.9 MV/cm), 3.2 V (4.0 MV/cm), 3.3 V (4.1 MV/cm), and 3.4 V (4.3 MV/cm) were applied to the 8-nm samples. The current was gradually decreased with time, and soft breakdown was observed before hard breakdown through the film. This phenomenon can be explained by the generation of trap sites in the film, where the generated defects create a percolation path along the trap sites [21]. The P–E characteristics post soft breakdown were examined to confirm the ferroelectricity, with the result that clear remanent polarization was obtained (see inset of Fig. 7(a)). Therefore, the hard breakdown time (tBD) of the film was extracted as the lifetime at which the current flow exceeds 10 A/cm2 , resulting in lower tBD at higher applied voltages. The tBD at 63% (T63) versus electric field for samples of both thicknesses were plotted in a log–log graph (Fig. 8). The tBD follows a power-law fit (tBD∝ V-n) for both samples, as commonly accepted [22]. The tBD of the 8-nm sample was longer than that of the 10-nm sample, which is in good agreement with the value of EBD in Fig. 6 while maintaining parallelism. The accelerated factor of the tBD from 3.5 V (4.4 MV/cm) to 2.0 V (2.5 MV/cm) for the 8-nm sample was extracted at approximately 1012, as shown in Fig. 8. Considering these effects, film thickness scaling results in a reliable hard breakdown when operating at 2.0 V using a 1T1C FeRAM array.

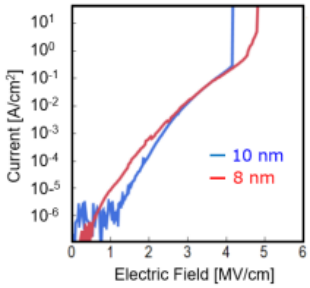

Fig. 6. J–E characteristics (2 V/s) of the 8-nm (red) and 10-nm (blue) samples using pristine single large MFM capacitors of area 1,000 μm2 each and comprising 1,000 capacitors (each of area 1 μm2) connected in parallel.

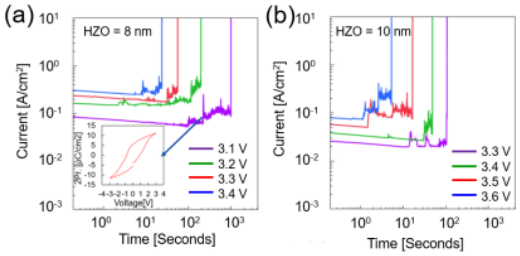

Fig. 7. Current–time trace measurements of the (a) 8-nm and (b) 10-nm samples using pristine single large MFM capacitors of area 1,000 µm2 each and comprising 1,000 capacitors (each of area 1 µm2) connected in parallel. The inset in (a) describes the P–E characteristics post soft breakdown during the current–time trace measurement on another device under the same test conditions.

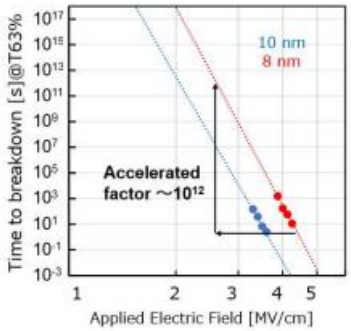

Fig. 8. The tBD at 63% (T63) versus electric field in a log–log graph for both 8-nm (red) and 10-nm (blue) samples. A total of 22 devices were tested for stress for each sample. Weibull slopes of 1.01 and 1.00 were used for the 8-nm and 10-nm samples plots, respectively.

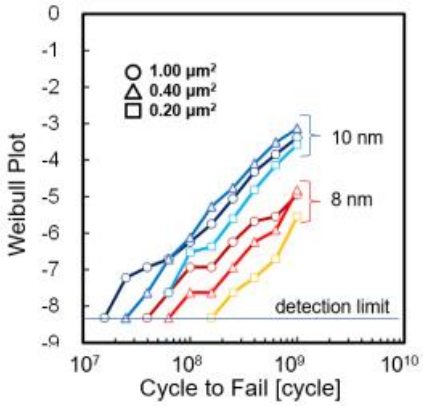

Fig. 9. Weibull fitting plot as a function of the number of cycles to failure for 4 kbits of the 8-nm and 10-nm samples at a capacitance area in a memory cell of 0.20, 0.40 and 1.00 µm2 with a same stress electric field of 4.4 MV/cm on both samples.

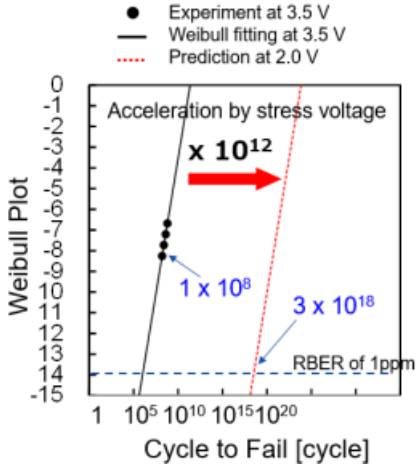

Fig. 10. Weibull fitting plot as a function of the number of cycles to failure for the 8-nm-thick sample at a capacitance area in a memory cell of 0.20 μm2 . The black line shows a fitting curve based on the experimental results at an operating voltage of 3.5 V. The red line shows a projection at 2.0 V using accelerated factor extracted from Fig. 8 [16].

C. Reliability characterization for 1T1C FeRAM array

The properties of the 1T1C FeRAM array using 8-nm and 10- nm samples consisting of TiN/HZO/TiN capacitors were previously reported in [17], [18]. The RBERs due to hard breakdown were investigated on both 8-nm and 10-nm samples using 4 kbits for capacitors with different capacitance areas of 0.20, 0.40, and 1.00 μm2 in a memory cell, as shown in Fig. 9. Cycling stress was applied with 4.4 MV/cm, 100 ns, and 85 °C as an accelerated condition. The cycle to failure of the earliest bit on the 8-nm sample was longer than that of the 10-nm sample in any capacitor size, which is in good agreement with the TDDB results in Fig. 8. The area dependence on the cycle to failure was clearly observed following the Poisson distribution [23]. The area dependence converged as the number of cycles increased, implying that the failure mechanism changed with increased cycling. One possible explanation for this phenomenon is that as the number of cycles increased, too many trap sites were generated in the film, obscuring the dependence on the area. The cycling tolerance for hard breakdown at an RBER of 1 ppm on the 8-nm sample was predicted under the operating conditions of 2.0 V and 100 ns at 85 °C at a capacitor area of 0.20 μm2 in the memory cell, as shown in Fig. 10. Considering the accelerated factor extracted from the TDDB results in Fig. 8, the value was projected to be 3.2 × 1018 . Lower cycling tolerance for hard breakdown was obviously predicted for the 10-nm sample using the data on Fig.8 and Fig.9 with a same method. (Not shown) For further reliability analyses, the retention and fatigue characteristics of the MFM capacitors need to be investigated. We characterized the retention characteristics using a single large capacitor in a previous study [17] and obtained negligibly small changes in polarization. In terms of the fatigue characteristics, the remanent polarization was observed to degrade by 30% during 109 cycles owing to the domain pinning in the MFM film [17]. For practical endurance behavior of 1T1C FeRAMs, we need to consider the degradation due to fatigue; nonetheless, enlarging the remanent polarization or increasing the sensitivity of SA would solve the problem.

IV. CONCLUSION

Our investigation focused on current research about HfO2-based ferroelectric devices, specifically examining the impact of film thickness. Our findings imply that the 1T1C FeRAM has the potential for increased cycle tolerance against hard breakdown and reduced operating voltage via the use of film thickness scaling technology. In order to ascertain the advantages of scaling the film thickness, we conducted a study to assess the dependability of MFM films with Hf0.5Zr0.5O2 thicknesses of 10-nm and 8-nm. The 8-nm sample exhibited a greater EBD in TZDB measurements, whereas TDDB measurements showed a longer tBD at the same stress electric field. These findings are consistent with prior studies [17], [18]. In addition, we conducted an experimental study to confirm the advantage of film thickness scaling in 1T1C FeRAM arrays. We used different HZO thicknesses of 8 nm and 10 nm, along with varying small capacitor areas (0.20, 0.40, and 1.00 μm2). This study is the

first to demonstrate a cycling tolerance value exceeding 1018 for hard break-down. The experiments were conducted at an operating voltage of 2.0 V and operating speed of 100 ns at 85 °C. The 8-nm sample, with consistent HZO thickness and capacitance area dependence, exhibited the highest cycling tolerance value. The use of a ferroelectric layer with a thickness less than 8 nm in 1T1C FeRAM enables a reduction in operating voltage or an enhancement in cycle tolerance. While achieving ferroelectricity in a thinner HZO requires a greater thermal budget [16], the CUB structure offers the benefit of an enhanced thermal budget. Nevertheless, the heightened leakage current of capacitors would restrict the scaling of film thickness and hinder the application of the optimal voltage to the capacitors, which are shared with the plate lines or bit lines. Conducting a continuous feasibility research on the dependability of the 1T1C FeRAM array, specifically focusing on fatigue and retention characteristics, is necessary for the practical implementation of different types of nonvolatile memory. This examination will be carried out in a future study.

REFERENCES

[1] T. S. Böscke et al., "Ferroelectricity in hafnium oxide thin films," Appl. Phys. Lett., vol. 99, no. 10, 2011, Art. no. 102903. DOI: 10.1063/1.363405.

[2] A. Toriumi et al., "Material perspectives of HfO2-based ferroelectric films for device applications," in Proc. IEEE Int. Electron Devices Meet. (IEDM), 2019. DOI: 10.1109/IEDM19573.2019.8993464.

[3] T. Mitmann et al., "Impact of oxygen on the performance of ferroelectric Hf0.5Zr0.5O2 based devices," in Proc. IEEE Int. Electron Devices Meet. (IEDM), 2019. DOI: 10.1109/IEDM13553.2020.9372097.

[4] S. Dünkel et al., "A FeFET based super-low-power ultra-fast embedded NVM technology for 22nm FDSOI and beyond," in Proc. IEEE Int. Electron Devices Meet. (IEDM), 2017. DOI: 10.1109/IEDM.2017.8268425.

[5] A. Sharma et al., "High speed memory operation in channel-last, backgated ferroelectric transistors," in Proc. IEEE Int. Electron Devices Meet. (IEDM), 2020. DOI: 10.1109/IEDM13553.2020.9371940.

[6] C. Sun et al., "First demonstration of BEOL-compatible ferroelectric TCAM featuring a-IGZO Fe-TFTs with large memory window of 2.9 V, scaled channel length of 40 nm, and high endurance of 108 cycles," in Proc. IEEE Symp. VLSI Technol., Kyoto, Japan, 2021, pp. 1–2.

[7] A. Tan et al., "Ferroelectric HfO2 memory transistors with high-κ interfacial layer and write endurance exceeding 1010 cycles," IEEE Electron Device Lett., vol. 42, no. 7, pp. 994–997, 2021, DOI: 10.1109/LED.2021.3083219.

[8] S. Fujii et al., "First demonstration and performance improvement of ferroelectric HfO2-based resistive switch with low operation current," in IEEE Symp. VLSI Technol., 2016. DOI: 10.1109/VLSIT.2016.7573413.

[9] B. Max et al., "Direct correlation of ferroelectric properties and memory characteristics in ferroelectric tunnel junctions," IEEE J. Electron Devices Soc., vol. 7, pp. 1175–1181, 2019. DOI: 10.1109/JEDS.2019.2932138.

[10] S. Fujii et al., "Improved state stability of HfO2 ferroelectric tunnel junction by template-induced crystallization and remote scavenging for efficient in-memory reinforcement learning," in Proc. IEEE Symp. VLSI Technol., 2020. DOI: 10.1109/VLSITechnology18217.2020.9265059.

[11] T. Francois et al., "Demonstration of BEOL-compatible ferroelectric Hf0.5Zr0.5O2 scaled FeRAM co-integrated with 130 nm CMOS for embedded NVM applications," in Proc. IEEE Int. Electron Devices Meet. (IEDM), 2019. DOI: 10.1109/IEDM19573.2019.8993485.

[12] J. Okuno et al., "SoC compatible 1T1C FeRAM memory array based on ferroelectric Hf0.5Zr0.5O2," in Proc. IEEE Symp. VLSI Technol., 2020. DOI: 10.1109/VLSITechnology18217.2020.9265063

[13] J. Okuno et al., "1T1C FeRAM memory array based on ferroelectric HZO with capacitor under bitline," IEEE J. Electron Devices Soc., vol. 10, pp. 29–34, 2022. DOI: 10.1109/JEDS.2021.3129279.

[14] M. Pesic et al., "Built-in bias generation in anti-ferroelectric stacks: Methods and device applications," IEEE J. Electron Devices Soc., vol. 6, pp. 1019–1025, 2018. DOI: 10.1109/JEDS.2018.2825360.

[15] S. Chang et al., "Anti-ferroelectric HfxZr1-xO2 capacitors for highdensity 3-D embedded-DRAM," in Proc. IEEE Int. Electron Devices Meet. (IEDM), 2020. DOI: 10.1109/IEDM13553.2020.9372011.

[16] K. Tahara et al., "Strategy toward HZO BEOL-FeRAM with low-voltage operation (≤ 1.2 V), low process temperature, and high endurance by thickness scaling," in Proc. IEEE Symp. VLSI Technol., Kyoto, Japan, pp. 1–2, 2021.

[17] J. Okuno et al., "High-endurance and low-voltage operation of 1T1C FeRAM arrays for nonvolatile memory application," in IEEE Int. Memory Workshp., 2021. DOI: 10.1109/IMW51353.2021.9439595.

[18] J. Okuno et al., "Demonstration of 1T1C FeRAM Arrays for Nonvolatile Memory Applications," in IEEE I 2021 20th International Workshop on Junction Technology (IWJT)., 2021. DOI: 10.23919/IWJT52818.2021.9609497.

[19] A. Sheikholeslami and P. G. Gulak, "A survey of circuit innovations in ferroelectric random-access memories," in Proc. IEEE, vol. 88, no. 5, pp. 667–689, 2000. DOI: 10.1109/5.849164.

[20] K. Schuegraf and Chenming Hu, "Effects of temperature and defects on breakdown lifetime of thin SiO2 at very low voltages," IEEE Trans. Electron Devices, vol. 41, no. 7, pp. 1227–1232, 1994. DOI: 10.1109/16.293352.

[21] K. Florent et al., "Investigation of the endurance of FE-HfO2 devices by means of TDDB studies," in Proc. IEEE Int. Reliab. Phys. Symp. (IRPS), 2018. DOI: 10.1109/IRPS.2018.8353634.

[22] E. Y. Wu et al., "Experimental evidence of TBD power-law for voltage dependence of oxide breakdown in ultrathin gate oxides," IEEE Trans. Electron Devices, vol. 49, no. 12, pp. 2244–2253, 2002. DOI: 10.1109/TED.2002.805606.

[23] L. Grenouillet et al., "Nanosecond Laser Anneal (NLA) for Si-implanted HfO2 Ferroelectric Memories Integrated in Back-End Of Line (BEOL)" in Proc. IEEE Symp. VLSI Technol., 2020. DOI: 10.1109/VLSITechnology18217.2020.9265061.